

Vortex-lattice formation and melting in a nonrotating Bose–Einstein Condensate

Gary Ruben,* David M. Paganin, and Michael J. Morgan
School of Physics, Monash University, Victoria 3800, Australia
 (Dated: January 2, 2008)

Numerical simulations of the interference of a three-way segmented nonrotating Bose–Einstein Condensate reveal the production of a honeycomb vortex lattice containing significant numbers of vortices and antivortices which, if confined within a trap, interact in complex ways over time. In contrast with nonlinear vortex production mechanisms previously described for BECs, the process here is primarily one of linear superposition, with initial vortex locations described by a linear theory of wave packet interference. The subsequent interaction dynamics, involving a rich vortex–antivortex chemistry, reveal a phase transition from an ordered to a disordered state.

PACS numbers: 03.75.Lm, 03.75.Dg, 03.75.Kk

I. INTRODUCTION

The production of vortices has attracted great interest in the study of Bose–Einstein Condensates (BECs) (see, e.g., [1, 2, 3, 4]). Typically, production has been through bulk rotation of the condensate cloud, such as with a “laser spoon” or by laser phase imprinting. These rotating systems form an Abrikosov lattice [5] of vortices with hexagonal symmetry. In contrast with the rotating BEC, in which the number of vortices is governed by the net angular momentum of the system, the nonrotating BEC can also give rise to vortices due to the reconciliation of initial random phase variations via the Kibble–Zurek mechanism [6].

Interference of two nonrotating BEC pieces with a repulsive nonlinearity, has also been shown to give rise to vortices [7, 8]. In this system, analogous to the Young’s two-pinhole interferometer, the interference fringes—also known as dark stripe solitons—decay via a “snake instability” into a string of vortices. This vortex formation mechanism relies on the nonlinearity of the BEC self interaction.

Recently Scherer et al. [9, 10] performed an experiment in which vortices were observed as a result of the interference of a three-way segmented BEC. An oblate spheroidal BEC was

formed in an asymmetric trap partitioned into three regions by shining a laser light sheet on the condensate (see Fig. 1). The partition walls were then removed at varying rates and vortices were sought after different elapsed times, during which the three pieces were allowed to expand and interfere. Both 2D and 3D numerical simulations of this experiment have also been performed by Carretero-González et al. [11].

In this report, we demonstrate with numerical simulations that vortices are produced by a three-segment BEC devoid of initial phase variations and show that this mechanism is, in contrast with the two-piece case, predicted by a linear theory, the development of which is related to previous work on the three-pinhole Young’s interferometer [12]. In contrast with Carretero-González et al. [11], we have not sought to replicate the aforementioned experiment exactly. By instead seeking true condensate ground-states, in order to remove initial phase variations, we aim to demonstrate that such phase variations are unnecessary for vortex formation. In addition, we demonstrate interference and vortex production in the absence of a confining transverse trap, thereby reducing the requirement for the nonlinear processes at play in two-fragment condensate interference, and hoping to improve the argument that the vortex generation mechanism for three pieces is, by contrast, primarily a linear process.

By slightly altering the initial conditions, primarily by increasing the intensity of the light sheet, we have also been able to generate significant numbers of vortices and antivortices. These large populations, produced in the trapped system, make it an excellent environment for the study of vortex dynamics. We see a phase transition of the topological defects in the order-parameter field during which the regular vortex–antivortex lattice melts into a disordered state. This defect phase transition could be characterized by a suitable order parameter of the defect field, which is a level removed from the order parameter of the BEC itself. We do not attempt such a description in this report. Following this defect phase transition, we observe a rich diversity of complex interactions by, for example, self-propelling vortex–antivortex dipoles (VADs) [11, 13, 14, 15, 16, 17], rotating vortex tripoles and quadrupoles [15, 16]. These interactions between vortices and vortex clusters in the condensate include dipole scattering and annihilation events.

The remainder of this report is structured as follows. In Sec. II we describe the numerical BEC model, focusing on

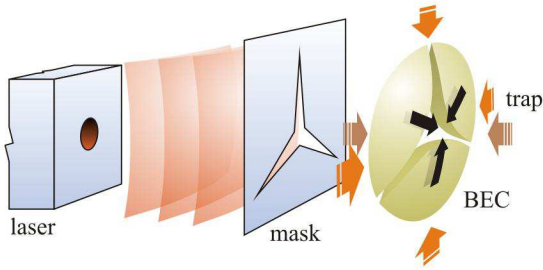


FIG. 1: (Color online) A laser-illuminated mask separates a pancake-shaped BEC, formed in an asymmetric trap, into three pieces. Upon removal of the illumination—and optionally the trap—the pieces interfere, forming a vortex lattice.

*Electronic address: gary.ruben@sci.monash.edu.au

the time-dependent and ground state models, the reduction from 3D to 2D, and a vorticity metric for the order parameter field. Next, we present the simulation results in Sec. III, highlighting the effects of light-sheet intensity, different light sheet geometries and phase variation between the condensate pieces in the trapped and untrapped cases, whilst making connections to the linear theory. We provide a visualization of the defect phase transition, and in Sec. IV, describe the rich vortex–antivortex dynamics which characterize the disordered state of the defect phase. Finally, we summarize our findings in Sec. V.

II. NUMERICAL MODEL

In this section we describe the derivation and parameters of the numerical model. We model an experiment similar to that conducted by Scherer et al. [9, 10].

Some distinguishing features of our simulation compared with the experiment and the modeling in Carretero-González et al. [11] are, firstly, that a ground state of the BEC system is established as a starting boundary condition for time evolution. Being a true ground state, no phase variation is allowed within or between the three pieces. We then optionally apply different relative phases to the three pieces following establishment of the ground state, in order to show the prediction of vortex production by the linear theory. In contrast, Carretero-González et al. [11] apply the experimentally determined chemical potential to their initial condition. The second distinguishing feature is the instantaneous removal of the light sheet at $t = 0$. In contrast, Scherer et al. [9, 10] remove the light sheet at varying finite rates, but report a maximum efficiency of vortex generation for the maximum observable rate of removal. Thirdly, we exclusively model the system in 2D. As such, our simulations are perhaps more applicable to pancake-shaped condensate clouds, in which the ratio of the axial to transverse trap frequencies is greater. A final difference is that we present simulations with and without the transverse trap to demonstrate that lack of transverse confinement is not an impediment to vortex production, consistent with predictions from the linear theory.

The evolution of the macroscopic wavefunction or order parameter Ψ of a BEC is governed by the Gross-Pitaevskii equation (GPE)

$$i\hbar\partial_t\Psi = \left[-\frac{\hbar^2}{2m}\nabla^2 + V(r, \theta, z) + NU_0|\Psi|^2 \right] \Psi, \quad (1)$$

where we have adopted cylindrical polar coordinates (r, θ, z) and time t . The GPE takes the form of the time-dependent Schrödinger equation with an additional nonlinear self-interaction term $NU_0|\Psi|^2\Psi$. Here $U_0 = 4\pi\hbar^2 a/m$ depends on the mass m of an atom of the atomic species (^{87}Rb in this case) and the s -wave scattering length a , which in this case is positive in order to permit the BEC pieces to expand and interfere. In our model $a = 5.77 \times 10^{-9}$ for ^{87}Rb [2]. The BEC contains N atoms and evolves within a trapping potential $V(r, \theta, z) = (m/2)(\omega^2 r^2 + \omega_z^2 z^2)$ with radial angular frequency ω and axial angular frequency ω_z . For the mo-

ment, this assumes that any light sheet is instantaneously removed at $t = 0$. We will discuss later the establishment of the ground state with the light-sheet potential $L(r, \theta)$ present, whence $V(r, \theta, z) = (m/2)(\omega^2 r^2 + \omega_z^2 z^2) + L(r, \theta)$ for $t < 0$.

Numerically, we employ the RK4IP scheme implemented in the XmdS software package [18]. This is a finite difference, split step, fourth order, adaptive Runge–Kutta method in the interaction picture.

A. Reduction from 3D to 2D

The production of vortices in pancake-shaped condensates may be numerically modeled in two rather than three spatial dimensions. The simplest model of such a system holds when the dimension $\lambda_z = [\hbar/(m\omega_z)]^{1/2}$ of the BEC ground state is much larger than the scattering length a [19]. Simplifying assumptions allow the transverse and z -components to be separated and nonlinear behavior along the z -dimension to be ignored. The z -dimension of the BEC is then independently treatable as a simple 1D harmonic oscillator problem, with a Gaussian ground state solution. Evaluating the Gaussian solution at $z = 0$ results in a multiplication factor γ for the number of atoms γN in the $z = 0$ plane.

More formally, with a view to evaluating γ , we apply the ansatz $\Psi(r, \theta, z) = \hat{\Psi}(r, \theta)\Phi_0(z) = \hat{\Psi}(r, \theta)\gamma^{1/2}\exp(-cz^2)$, where c is a constant, such that $\Psi(r, \theta, z)$ is a product of the transverse solution $\hat{\Psi}(r, \theta)$ and the well-known ground-state solution $\Phi_0(z) = (\pi\lambda_z^2)^{-1/4}\exp[-z^2/(2\lambda_z^2)]$ to the 1D time independent Schrödinger equation

$$E\Phi = \left(-\frac{\hbar^2}{2m}\partial_z^2 + \frac{1}{2}m\omega_z^2 z^2 \right) \Phi. \quad (2)$$

The factor γ may be found by evaluating the ground state at $z = 0$ and applying the normalization condition $\int_{-\infty}^{\infty} |\Phi_0(z)|^2 dz = 1$.

The Laplacian operator in Eq. (1) is then separated into its transverse and axial components, $\nabla_{\perp}^2 \equiv \partial_x^2 + \partial_y^2$ and ∂_z^2 respectively, thus $\nabla^2 \equiv \nabla_{\perp}^2 + \partial_z^2$. Noting that the terms on the RHS of Eq. (2) now also appear in Eq. (1), they are replaced in Eq. (1) by the LHS of Eq. (2). Subsequent evaluation of Eq. (1) at $z = 0$ results in the 2D equation

$$i\hbar\partial_t\hat{\Psi} = \left(-\frac{\hbar^2}{2m}\nabla_{\perp}^2 + \frac{m}{2}\omega^2 r^2 + E + \gamma NU_0|\hat{\Psi}|^2 \right) \hat{\Psi}, \quad (3)$$

where E may be interpreted as a change in the chemical potential of the condensate. The probability density is gauge invariant with respect to this term, so we apply the transform $\hat{\Psi} \rightarrow \hat{\Psi}\exp(-iEt/\hbar)$ to eliminate E .

B. Establishing the ground state

The ground state is the eigenfunction solution of the time independent GPE, where the potential term now includes the light-sheet. We seek the ground state for use as the initial

condition of the time dependent GPE. Numerically, this is obtained by evolving a modified version of the time dependent wavefunction, obtained by Wick rotating the time variable in the energy operator, according to $t' = -it$ (see, e.g., [20]). This technique, in which the wave equation is transformed into a diffusion equation, is often termed “evolution through imaginary time”. Note that Wick rotation is not performed on the wavefunction $\hat{\Psi}$. Subsequently dropping the prime from t' , the resulting equation is

$$\hbar\partial_t\hat{\Psi} = \left(\frac{\hbar^2}{2m}\nabla_{\perp}^2 - \frac{m}{2}\omega^2 r^2 - L(r, \theta) + \mu - \gamma NU_0 |\hat{\Psi}|^2 \right) \hat{\Psi}, \quad (4)$$

where the real-valued parameter μ has been added because the system energy acquires a constant value associated with the number of atoms in the condensate. In the limit $t \rightarrow \infty$, μ is identified as the chemical potential. In this limit, $\partial_t\hat{\Psi} \rightarrow 0$ and Eq. (4) approaches the time-independent GPE (see, e.g., [4]). The time evolution is performed by iteratively performing time steps according to the chosen scheme (e.g. fourth-order Runge–Kutta) followed by renormalization of the wavefunction to ensure there are N atoms in the condensate. Because the system being modeled is highly nonlinear—i.e. $g \gg 1$ where $g \equiv 8\gamma N\pi\alpha$ is the coefficient of the nonlinear term $|\hat{\Psi}|^2 \hat{\Psi}$ in the GPE—the appropriate initial condition is the solution to the Thomas-Fermi limit of the GPE [21, 22]. We use this limit as the initial condition in our simulations, which provides rapid convergence to the true ground state. However, the stability of the method permits other choices of initial condition.

C. Vorticity measure

We define a vorticity metric for the order parameter field $\hat{\Psi}$ according to

$$\text{Vorticity} = \frac{1}{V} \iint |\nabla \times \mathbf{j}| dx dy, \quad (5)$$

where the integral represents integration over the numerical field of volume V , and \mathbf{j} is the probability current $\mathbf{j} \equiv (\hat{\Psi}^* \nabla \hat{\Psi} - \hat{\Psi} \nabla \hat{\Psi}^*) \hbar / (2m)$.

This metric is similar to the usual vorticity measure in fluids $\omega = \nabla \times \mathbf{v}$, of the velocity field $\mathbf{v} = \mathbf{j}/\rho$ where $\rho = |\hat{\Psi}|^2$ is the local density. It is equivalent to ω multiplied by the local density ρ . By not dividing by ρ , extra weighting is conferred upon vortices located within a locally increased density over vortices in regions of lower density. The metric sums the modulus of the local measure over the whole field.

III. RESULTS

In Fig. 2 we present simulation snapshots for the segmented BEC showing the initial state, the lattice, and later stages that, in the trapped cases, succeed the defect phase transition. For corresponding movies, see [23]. The intensity of the laser

light sheet relative to the trap is represented by a dimensionless quantity I_0 , where the trap potential contour plots (shown in false color to the left of the time series) indicate the magnitude relative to the trap. We have chosen to present results for $I_0 = 0.3$ or $I_0 = 0.8$ as these values allow exposition of the different behaviors of poorly and well separated BEC pieces, respectively. The upper time series show the evolution of the BEC beginning from a true global ground state. Probability density and phase are also shown in Fig. 2. The expansion and interference occurs both (a) within a confining harmonic trap following instantaneous removal of the light sheet, and (b) in the absence of a transverse confining trap. In the latter case, the condensate would expand beyond a finite simulation region. To allow for this, a circular damping function absorbs the outward propagating matter, leading to the darkened outer region in this case. Since these are 2D simulations, and as such are applicable to pancake-shaped condensates, experimental realization would most likely require maintenance of the axial trap in both cases.

Scherer et al. [9, 10] observed vortices consistent with production by the Kibble-Zurek mechanism. They reported that 10% of nonsegmented condensates contain vortices. In our simulations, by starting from a ground state, no vortices may be produced by this mechanism.

Previous work [12] has shown that the linear interference of three expanding monochromatic spherical waves generates a distorted honeycomb vortex–antivortex (VA) lattice. In the Appendix, we present a related linear theory for the case of three Gaussian wave packets, evolving in two dimensions of space and one of time, clarifying the effect of source phase variation on the predicted vortex locations. In this case, an infinite, regular honeycomb VA lattice is formed, with a Gaussian probability density envelope. The formation of vortices by a three-piece BEC may be understood as arising from the same mechanism, albeit now in a highly nonlinear system.

The linear theory applies most directly to the untrapped system. For observing interaction dynamics, the trap presence must be maintained. However, if the interference is instead performed with the transverse trap switched off, experimental measurement of the position of any central vortex with respect to the center and lattice parameter should allow determination of the phases of the initial BEC pieces to within a global phase factor. Figures 2(b) and (d) show the formation of an extremely regular lattice, which compares favorably with that formed by linear superposition in Fig. 3.

If the three BEC pieces are sufficiently isolated from each other, they may acquire random phases with respect to one another [24]. Scherer et al. [9] describe the presence or absence of a central vortex according to reconciliation of these phases. The linear theory instead describes an equivalent effect, which predicts the presence of a central vortex as resulting from translation of the lattice as a whole. Röhrli et al. [24] state that the pieces are “virtually degenerate”, allowing them to be treated as coherent pieces whose relative phases may vary randomly. For a lower intensity light sheet, tunneling through the light-sheet walls ensures that the phases of the separate pieces remain coupled. The interference pattern is said to become “locked”. In our case, the lattice translation

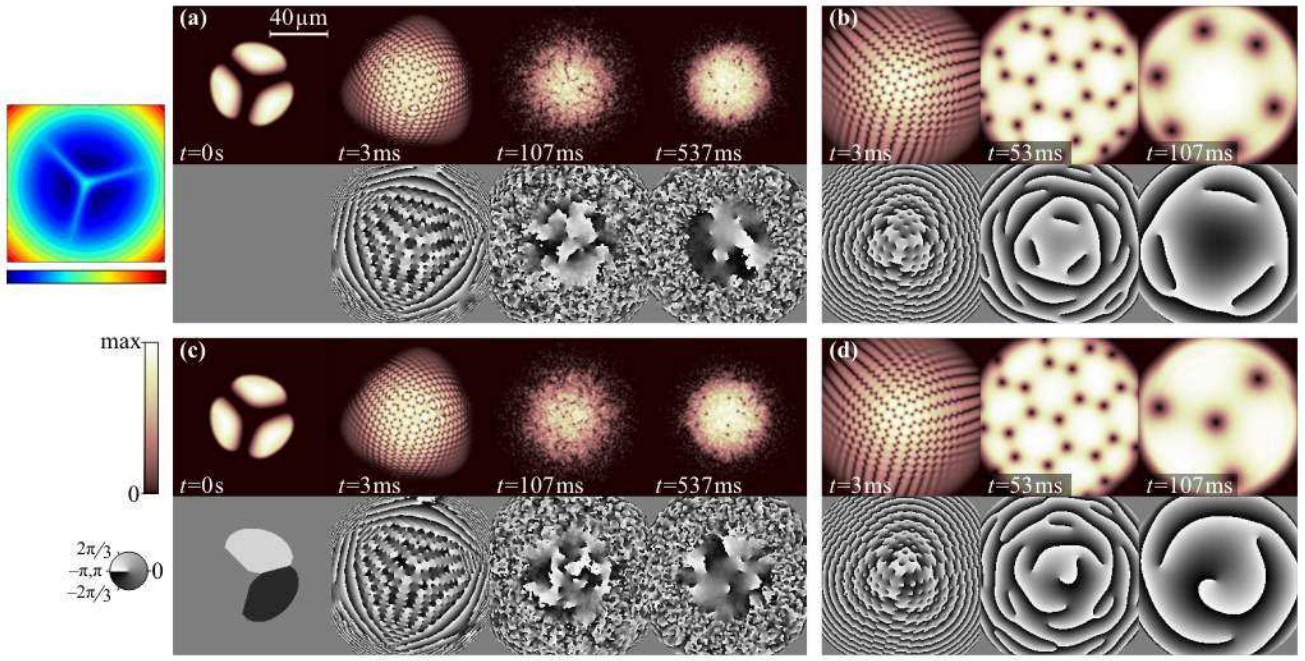


FIG. 2: (Color online) Amplitude (sepia) and associated phase plots (gray scale) for the ground-state trap potential shown as a contour-plot at left, which is a 2D harmonic trap with a superposed three-way light sheet of dimensionless amplitude $I_0 = 0.8$. (a) Three-segment BEC interference with a harmonic confining trap showing progression from the ground state, through lattice formation to a late-stage characterized by complex vortex–antivortex (VA) dynamics. (b) Honeycomb lattice formation and free expansion in the absence of a confining trap. The dark outer circular envelope results from a damping term used in the numerical scheme, which prevents reflections from the boundary of the finite numerical grid. (c-d) The initial piece phases are rotated to 0 , $2\pi/3$ and $-2\pi/3$. The effect is to shift the lattice so that an antivortex is centered on the trap or region of focus.

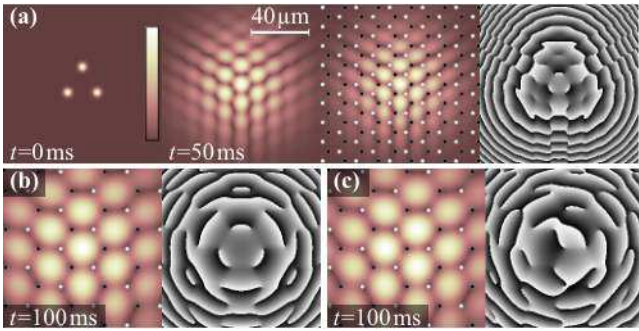


FIG. 3: (Color online) Three linearly superposed wave packets lying at the corners of an equilateral triangle [cf. Figs. 2(b) and (d)]. The amplitude, with analytically determined vortices (dark) and antivortices (light) overlaid [see Eqs. (A10) and (A11)], and phase of Eq. (A2) are shown. (a) Equal-phase wave packets shown at 0 ms, after interference at 50 ms (with and without the overlaid lattice), and (b) after 100 ms. (c) Phases 0 , $2\pi/3$ and $-2\pi/3$ cause a lattice translation.

becomes locked in an equivalent sense to give the result in Figs. 2(a) and (b). To simulate the effect of decoupling between the pieces, we apply global phase factors by rotating the phase of the BEC pieces, following establishment of the ground state but prior to time evolution.

In Figs. 2(c-d), the relative phases of two of the regions

have been rotated from 0 to $2\pi/3$ and $-2\pi/3$, as shown in the $t = 0$ s phase plot. The $t = 53$ ms and $t = 107$ ms cases without a transverse trap show a vortex at the center. This may be understood by evaluating the predicted vortex locations using the linear theory. To illustrate this, Fig. 3 provides linear simulation results for the equal [Figs. 3(a-b)] and rotated [Fig. 3(c)] phase cases for the model described in the Appendix. For these examples, the source positions r_2 and r_3 , and the momentum uncertainty Δp were determined by fitting Gaussian profiles to the leading (innermost) edges of the probability density of the three BEC pieces at $t = 0$ for the $I_0 = 0.8$ case, i.e. from the first frame in Fig. 2(a). Because the model assumes that the BEC pieces are well described by circularly-symmetric Gaussian pieces, which is not the case here, this approach was found to be better than fitting to the whole BEC-pieces. However, because of this departure, illustrated by the poor match of the lattice scale to that of the nonlinear results, the linear model is best applied qualitatively. Although the nonlinear dynamics of the BEC do not allow the analytically predicted vortex locations to be mapped directly onto the nonlinear simulation results, the linear theory nevertheless provides useful predictions of the generation of the central vortex and the lattice symmetry.

If the phases are such that a vortex is created sufficiently close to the center of the trap, in the case where few other vortices are produced, such as when the wall heights are low [as in Figs. 4(a-d)], the vortex may migrate to take up residence

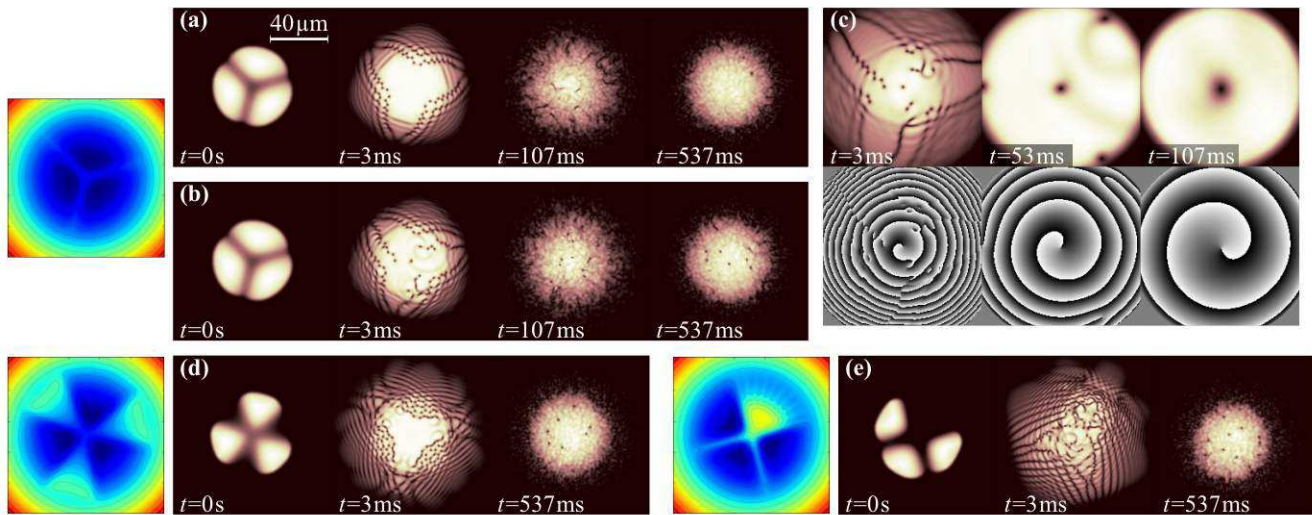


FIG. 4: (Color online) Amplitude (sepia) and associated phase plots (grays) for light sheets characterized by the trapping potentials shown as adjacent contour plots. (a-c) When compared with Fig. 2, the lower intensity light sheet ($I_0 = 0.3$) allows vortices to propagate outwards with the condensate matter. In (a), the central region of the lattice is left devoid of vortices. In the trapped (b) and untrapped (c) cases—in which the relative phases of the initial pieces are set to 0 , $2\pi/3$ and $-2\pi/3$ —the central vortex is clearly visible. (d-e) Two alternative arrangements with (d) propeller-shaped pieces, and (e) pieces at three corners of a square are discussed in the main text.

in the center of the trap. Figure 4(b) illustrates this behaviour. Since phase gradients and associated flows cancel there, any resident vortex occupies a privileged position and is allowed to remain there until perturbed by a local change, such as that caused by the motion of a passing vortex.

The vorticity metric is plotted against time for four different initial conditions in Fig. 5(a). Figures 5(b-c), which resemble jellyfish, are time-series plots of the vortices in the side-on condensate slices. Initial formation of the regular vortex-antivortex lattice forms the *jellyfish bell*. Subsequently, the regular lattice melts during the period corresponding to the underside of the jellyfish bell, as the condensate matter washes back towards the center due to confinement by the harmonic trap. This melting may be understood as a defect phase transition from an ordered to a disordered state. During the early stages following the transition, the high population of vortices and antivortices promotes a high interaction rate characterized by a rich variety of highly dynamical vortex “chemistry” reactions. VA annihilation reduces the vortex population to a level where the reaction rate slows and dynamics involving VA dipoles begin to dominate, characterized by the trailing *jellyfish tentacles* at this later stage. The washing in and out is roughly circularly symmetric, cyclically increasing and decreasing the probability density in the center.

The global oscillations visible in (a) are due to the vorticity measure giving extra weight to vortices embedded in a locally increased probability density, consistent with the cyclic motion. From (b) and (c) we see that the vortices themselves are carried in and out by the bulk motion of the condensate matter, presumably changing the interaction/chemical-reaction rate in turn. The interaction dynamics are discussed in detail in Sec. IV.

A lower wall height results in the pieces starting closer to-

gether. In the linear theory in [12], correspondingly smaller r values generate smaller numbers of vortices. This is clearly illustrated by the smaller vorticity values in (a) and the reduced population of vortices in (c) over (b). In Figs. 4(a-b), we see that the matter expanding from the center carries most of the vortices to the outer parts of the trap as the lattice is forming, where they may be lost altogether, further reducing the vortex population.

The propeller shape in Fig. 4(d) is included to show an alternative mask, which also produces BEC pieces at 120° angles to each other, but which pushes the centers of the condensate pieces further apart. Accordingly, higher numbers of vortices are predicted by the BEC created from this mask. Indeed, this is the case, as can be seen by comparing the bottom two results in Fig. 5(a), which plot vorticity for the same light sheet intensity $I_0 = 0.3$ for the two 120° alternatives.

In the linear theory in [12], the maximum number of vortices is predicted for a source arrangement in which the pieces are initially arranged at three corners of a square. This prediction guided investigation of a new source configuration, shown in Fig. 4(e), which may be realized by a cross-shaped light sheet mask with one quadrant open to the passage of light from the illuminating laser. Confirmation of the prediction is apparent by comparing the top two results in Fig. 5(a), which are for the same light-sheet intensity. In fact, the spacing of the condensate centroids for the 90° arrangement is smaller than for the 120° case. Thus the angular arrangement more than offsets the decrease in vorticity-generating capacity caused by reducing the piece spacing. Whilst we have shown a geometry with an increased capacity to generate vortices, it is possible that nonlinearity causes the absolute maximum to be achieved for another angle close to 90° . The initial asymmetry of the condensate centroid with respect to the trap results

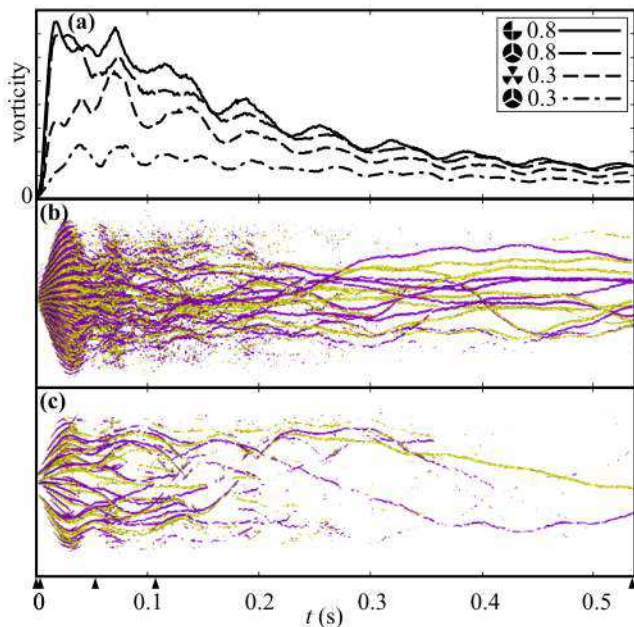


FIG. 5: (Color online) Vorticity plots for selected BEC segmentation schemes with a harmonic trap. Small arrows along the time axis correspond to the times selected in Figs. 2 and 4. (a) Vorticity measure [Eq. (5)] for $I_0 = 0.3$ and 0.8 and for sources at three corners of an equilateral triangle, a square and propeller shaped schemes (see main text). (b) Vortices (dark) and antivortices (light) generated from the equilateral triangle scheme with $I_0 = 0.8$. (c) Fewer vortices are produced with a lower intensity $I_0 = 0.3$ light sheet.

in the merged condensate oscillating back and forth along the initial mirror symmetry plane, in addition to the global oscillation mode.

A possible explanation for Scherer et al. [9] not observing the production of large numbers of vortices along with a regular lattice in experiments may be the use of light-sheet intensities more consistent with our lower intensity results. Blurring and possible nonuniformity of the light-sheet walls is related to the size and manufacturing process used for the mask—attention to the design of the mask optics and optical path may permit the creation of more uniform, sharper walls, leading to the lattice structures we see in simulations. Also, real experimental initial conditions with a non-zero-temperature chemical potential introduce some phase randomness which would disrupt the lattice.

IV. VORTEX DYNAMICS

In this section we provide a phenomenological description of the rich dynamics of the VA interactions seen in the trapped condensate following the phase transition to the disordered state. These are strikingly apparent in the accompanying movies [23].

The dynamics described in this section will be exhibited primarily in 2D pancake-shaped condensates. In 3D, vortices are string-like objects, either forming closed loops (e.g., ring

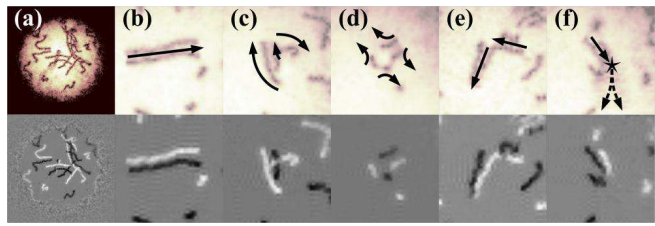


FIG. 6: (Color online) Vortex interaction dynamics. In the lower frames vortices (dark) and antivortices (light) are shown. (a) Vortex trails corresponding to the range $t=323$ – 429 ms for the 120° , $I_0 = 0.8$ arrangement. (b) A propagating vortex–antivortex dipole (VAD). (c) Vortex–vortex–antivortex tripole rotating through 90° . (d) Two VADs meet to form a quadrupole. VA partners are exchanged and the new VADs move off orthogonally. (e) A VAD meets a lone vortex. The antivortex exchanges its vortex partner and the new VAD moves off on a new trajectory. (f) VA annihilation resulting from passing by a lone vortex.

solitons) or terminating at two points on the condensate surface [4, 25]. In this case, the interaction dynamics are instead characterized by string intercommutation or formation of smaller loops.

Most of the BEC vortex literature has focused on vortices (or antivortices) in rotating traps, in which antivortices (vortices) are expelled from the condensate. The complex interactions described here instead rely on the presence of a population of vortices and antivortices and hence are best observed in a nonrotating system. Interfering condensates comprised of two, three, or more pieces will all generate the required conditions, provided they are nonrotating. Experimentally, phase contrast imaging with detuned light may leave the BEC sufficiently undisturbed to allow observation of these dynamics [26].

A vortex generates a local circulating velocity field and associated phase gradient which falls off rapidly with distance. Another vortex or antivortex in this field experiences a force in the direction of flow [13]. Similarly, VADs travel at a velocity determined by their distance apart. In Fig. 6(a), the paths of several VADs, are shown over a 106 ms period. The dipoles in which the partners are more widely spaced have shorter paths, illustrating the predicted behavior (see also accompanying movies [23]). In contrast, rotating vortex–vortex (or antivortex–antivortex) molecules are rarely and only fleetingly seen. Two equal-charge vortices can circulate around a common point, midway between them, like a facing pair of figure skaters. However, these structures have been shown to be unstable in radiative media [1, 27] and would also be disturbed by the more mobile VADs, or prevented from rotating by (countering) field gradients due to the presence of nearby antivortices (vortices).

The dynamical behavior of both vortex tripoles and quadrupoles [15, 16] are shown in Figs. 6(c) and (d), respectively. The net angular momentum of the tripole causes it to rotate through 90° . In (d), a rare event is shown, in which two counter-propagating VADs approach and momentarily meet, forming a quadrupole, before exchanging partners and moving off orthogonally to the original directions. In (e), a VAD

approaches a stationary vortex, which is swapped for the partnered vortex. The new VAD continues on a new trajectory.

The spacing of VADs changes in response to local field gradient perturbations, causing them to slow, speed up, separate completely, or annihilate. An example of annihilation, promoted by the proximity of another vortex, is shown in (f). Following the annihilation, scattered remnant waves travel ahead of the event location, dissipating the residual VAD kinetic energy. Vortices residing in the outer parts of the trap spiral helically about the center in a right-hand screw sense. Antivortices spiral in the opposite sense and are therefore likely to meet the aforementioned vortices. These often form VADs, which then move inward toward the trap center.

V. CONCLUSION

We have shown that, in contrast with the vortex creation mechanism from a two fragment interfering BEC, a three frag-

ment BEC combines to form a honeycomb vortex lattice by a primarily linear interference process. If the BEC subsequently remains trapped, the lattice undergoes a phase transition to a disordered state, characterized by a rich diversity of vortex interactions. If instead, the transverse trap component is removed, the honeycomb lattice expands and is maintained in form. The experimentally unobservable initial phases of the pieces manifest as a translation of the lattice.

Acknowledgments

The authors thank S. Clarke for helpful discussions. G.R. is supported by an Australian Postgraduate Award. D.M.P. acknowledges support from the Australian Research Council.

-
- [1] L. M. Pismen, *Vortices in Nonlinear Fields: From Liquid Crystals to Superfluids, From Non-Equilibrium Patterns to Cosmic Strings* (Oxford University Press, Oxford, 1999).
- [2] F. Dalfovo, S. Giorgini, L. P. Pitaevskii, and S. Stringari, *Rev. Mod. Phys.* **71**, 463 (1999).
- [3] A. L. Fetter and A. A. Svidzinsky, *J. Phys.: Condens. Matter* **13**, 135 (2001).
- [4] A. Minguzzi, S. Succi, F. Toschi, M. P. Tosi, and P. Vignolo, *Phys. Rep.* **395**, 223 (2004).
- [5] A. A. Abrikosov, *Sov. Phys. JETP* **5**, 1174 (1957).
- [6] J. R. Anglin and W. H. Zurek, *Phys. Rev. Lett.* **83**, 1707 (1999).
- [7] Y. S. Kivshar and B. Luther-Davies, *Phys. Rep.* **298**, 81 (1998).
- [8] D. L. Feder, M. S. Pindzola, L. A. Collins, B. I. Schneider, and C. W. Clark, *Phys. Rev. A* **62**, 53606 (2000).
- [9] D. R. Scherer, C. N. Weiler, T. W. Neely, and B. P. Anderson, *Phys. Rev. Lett.* **98**, 110402 (2007).
- [10] D. R. Scherer, Ph.D. thesis, University of Arizona (2007).
- [11] R. Carretero-González, B. P. Anderson, P. G. Kevrekidis, D. J. Frantzeskakis, and C. N. Weiler, eprint arXiv:0711.0375v1 (2007).
- [12] G. Ruben and D. M. Paganin, *Phys. Rev. E* **75**, 66613 (2007). G. Ruben and D. M. Paganin, *Phys. Rev. E* **76**, 029901(E) (2007).
- [13] P. Nozières and D. Pines, *The Theory of Quantum Liquids, Volume II: Superfluid Bose Liquids* (Addison-Wesley, 1990).
- [14] L. C. Crasovan, V. Vekslerchik, V. M. Pérez-García, J. P. Torres, D. Mihalache, and L. Torner, *Phys. Rev. A* **68**, 63609 (2003).
- [15] M. Möttönen, S. M. M. Virtanen, T. Isoshima, and M. M. Salomaa, *Phys. Rev. A* **71**, 33626 (2005).
- [16] V. Pietilä, M. Möttönen, T. Isoshima, J. A. M. Huhtamäki, and S. M. M. Virtanen, *Phys. Rev. A* **74**, 23603 (2006).
- [17] A. Klein, D. Jaksch, Y. Zhang, and W. Bao, *Phys. Rev. A* **76**, 43602 (2007).
- [18] *XmDS* (2007), eXtensible multi-dimensional Simulator. Retrieved from <http://www.xmDS.org> on 9 May 2007.
- [19] B. Tanatar, A. Minguzzi, P. Vignolo, and M. P. Tosi, *Phys. Lett. A* **302**, 131 (2002).
- [20] M. L. Chiofalo, S. Succi, and M. P. Tosi, *Phys. Rev. E* **62**, 7438 (2000).
- [21] M. Holland and J. Cooper, *Phys. Rev. A* **53**, 1954 (1996).
- [22] W. Bao, D. Jaksch, and P. A. Markowich, *J. Comp. Phys.* **187**, 318 (2003).
- [23] See EPAPS Document No. xxxxx for movies corresponding to Figs. 2(a), 4(b) and a trapped two-piece BEC. For more information on EPAPS, see <http://www.aip.org/pubservs/epaps.html>.
- [24] A. Röhrl, M. Naraschewski, A. Schenzle, and H. Wallis, *Phys. Rev. Lett.* **78**, 4143 (1997).
- [25] L. D. Carr and C. W. Clark, *Phys. Rev. A* **74**, 43613 (2006).
- [26] L. D. Turner, K. P. Weber, D. Paganin, and R. E. Scholten, *Opt. Lett.* **29**, 232 (2004).
- [27] N. P. Proukakakis, N. G. Parker, D. J. Frantzeskakis, and C. S. Adams, *J. Opt. B* **6**, S380 (2004).
- [28] B. H. Bransden and C. J. Joachain, *Quantum Mechanics* (Pearson Education, 2000), chap. 2, p. 65, 2nd ed.

APPENDIX A: VORTEX LATTICE PRODUCTION

In this Appendix we provide an analytical description of the vortices generated through linear superposition of three equal-mass sources expanding from concentrated Gaussian distributions. The exposition here follows the approach reported in [12] which studied the vortices in the interference pattern from the Young's three-pinhole interferometer. In that work, an analytical description of the far-field vortex locations was derived as a function of source arrangement for three equal-amplitude complex scalar waves represented as either spherical waves or pinhole sources. A representation in terms of a discrete parameter space arose, allowing estimates of the number of vortices—shown to relate to the information capacity of a beam—and the description of a natural coordinate system in terms of a family of hyperbolas.

Consider three Gaussian wave packets, each of unit mass, whose position expectation values are stationary and centered about coordinates $\mathbf{r}_1 \equiv \mathbf{0}, \mathbf{r}_2, \mathbf{r}_3$. This is shown in the po-

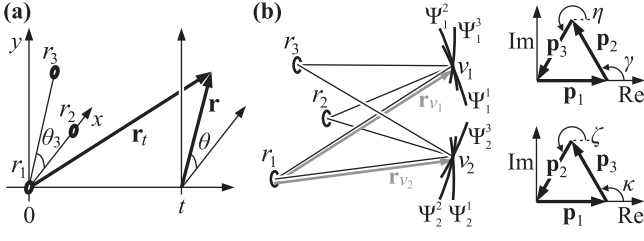


FIG. 7: (a) Coordinate system. Three sources lie in the xy -plane. Vortex positions are parameterized by polar coordinates (r, θ) at time t where \mathbf{r}_t is a 2+1D position vector. (b) Phasor construction of three interfering waves. Two possible phasor orderings, corresponding to a vortex and antivortex, may be produced by three given source wave-functions $\Psi_v, s \in \{r_1, r_2, r_3\}, v \in \{v_1, v_2\}$.

lar coordinate system schematic, Fig. 7(a). The normalized probability amplitude from a source lying at the origin, as a function of position \mathbf{r} and time t is given by [28]

$$\Psi(\mathbf{r}, t) = \frac{\pi^{-1/2} \Delta p / \hbar}{1 + i(\Delta p)^2 t / (m\hbar)} \exp\left(\frac{-(\Delta p / \hbar)^2 |\mathbf{r}|^2}{2[1 + i(\Delta p)^2 t / (m\hbar)]}\right), \quad (\text{A1})$$

where m is the mass of an atom of the atomic species, Δp is the momentum uncertainty that defines the wave packet width, and $\mathbf{r}_t = (\mathbf{r}, t)$ is a 2+1D position vector covering the xy -plane, whose origin lies at $(\mathbf{r}, t) = (\mathbf{0}, 0)$. The total probability amplitude arising from the three sources is then

$$\Psi(\mathbf{r}, t) = \sum_{j=1}^3 \frac{\pi^{-1/2} \Delta p / \hbar}{1 + i(\Delta p)^2 t / (m\hbar)} \times \exp\left(\frac{-(\Delta p / \hbar)^2 |\mathbf{r} - \mathbf{r}_j|^2}{2[1 + i(\Delta p)^2 t / (m\hbar)]} + i\phi_j\right), \quad (\text{A2})$$

where $|\mathbf{r} - \mathbf{r}_j| \equiv \sqrt{(x - x_j)^2 + (y - y_j)^2}$ is the distance from the j th source to a given observation point (\mathbf{r}, t) and ϕ_j is the relative phase of the j th source. Separating the amplitude and phase terms of the wave field components $\Psi_j(\mathbf{r}, t) = A_j(\mathbf{r}, t) \exp[i\chi_j(\mathbf{r}, t)]$, we get

$$A_j(\mathbf{r}, t) = \frac{\pi^{-1/2} \Delta p / \hbar}{1 + i(\Delta p)^2 t / (m\hbar)} \exp\left(\frac{-(\Delta p)^2 m^2 |\mathbf{r} - \mathbf{r}_j|^2}{2[(\Delta p)^4 t^2 + m^2 \hbar^2]}\right), \quad (\text{A3})$$

and

$$\chi_j(\mathbf{r}, t) = \frac{(\Delta p)^4 m t |\mathbf{r} - \mathbf{r}_j|^2}{2[(\Delta p)^4 t^2 \hbar + m^2 \hbar^3]} + \phi_j. \quad (\text{A4})$$

Vortices lie at points of the phase $\chi(\mathbf{r}, t)$, at which a line integral along a closed path Γ about such a point evaluates to a nonzero value. More formally $\oint_{\Gamma} d\chi = 2\pi n$ for some integer $n \neq 0$. At any point coinciding with a vortex core, the phasors $\mathbf{p}_1, \mathbf{p}_2, \mathbf{p}_3$ corresponding to the three wave packets, must sum to zero. Equivalently, Eq. (A2) is equated to zero. With reference to Fig. 7(b), if the phasors are of equal length—corresponding to equal amplitude contributions from the three sources—an equilateral triangle is formed, allowing the angles at the vertices to be specified simply.

As the amplitude contributions from the sources are not unconditionally equal we must make an appropriate approximation to the amplitude term. By restricting consideration to some finite region of space defined by $|\mathbf{r} - \mathbf{r}_j| \leq |\mathbf{r}_{\max} - \mathbf{r}_j|$, the exponential term in Eq. (A3) will be approximately unity provided its argument is small, or $(\Delta p)^4 t^2 + m^2 \hbar^2 \gg (\Delta p)^2 m^2 |\mathbf{r}_{\max} - \mathbf{r}_j|^2 / 2$. For a given \mathbf{r}_{\max} , this is always true after sufficient time has elapsed. The amplitude term may now be factored out of the probability amplitude expression. Expanding the term $|\mathbf{r} - \mathbf{r}_j|^2 \equiv r^2 - 2\mathbf{r} \cdot \mathbf{r}_j + \mathbf{r}_j \cdot \mathbf{r}_j$ and remembering that $\mathbf{r}_1 = \mathbf{0}$, the probability amplitude $\Psi(\mathbf{r}, t)$ from Eq. (A2) vanishes when

$$1 + \exp\left\{i\left[\alpha\left(r_2^2 - 2r_2 r \cos\theta\right) + \phi_2\right]\right\} + \exp\left\{i\left[\alpha\left(r_3^2 - 2r_3 r \cos(\theta - \theta_3)\right) + \phi_3\right]\right\} = 0, \quad (\text{A5})$$

where $\alpha = m\hbar t / [2(\hbar t)^2 + 2m^2(\hbar/\Delta p)^4]$. The three summands are associated with the three phasors in Fig. 7(b). Whereas the first summand, 1, is uniquely identified with the horizontal phasor, the association of the sources with the other two phasors allows two permutations, corresponding to the two phasor diagrams; one for each vortex, v_1 and v_2 . In fact one will be a vortex and the other an antivortex.

The arguments of the two exponentials in Eq. (A5) are denoted by γ and η , respectively. These phase angles are uniquely defined to within an integer multiple of 2π , so that:

$$\gamma = \alpha\left(r_2^2 - 2r_2 r \cos\theta\right) + \phi_2 = \frac{2\pi}{3} + 2m\pi, \quad (\text{A6a})$$

$$\eta = \alpha\left(r_3^2 - 2r_3 r \cos(\theta - \theta_3)\right) + \phi_3 = \frac{4\pi}{3} + 2n\pi, \quad (\text{A6b})$$

where m and n are integers. The association of the m and n indices with the vertices is arbitrary. The choice is made here to match m with r_2 and n with r_3 . The alternative phasor association is thus

$$\zeta = \alpha\left(r_2^2 - 2r_2 r \cos\theta\right) + \phi_2 = \frac{4\pi}{3} + 2m\pi, \quad (\text{A7a})$$

$$\kappa = \alpha\left(r_3^2 - 2r_3 r \cos(\theta - \theta_3)\right) + \phi_3 = \frac{2\pi}{3} + 2n\pi. \quad (\text{A7b})$$

Forming the fraction γ/η or ζ/κ yields

$$\frac{r_3}{r_2} \left(\cos\theta_3 + \tan\theta \sin\theta_3\right) = \frac{r_3^2 - \beta N(n)}{r_2^2 - \beta M(m)}, \quad (\text{A8})$$

where $\beta = 1/(3\alpha) = 2[(\hbar t)^2 + m^2(\hbar/\Delta p)^4]/(3m\hbar t)$. For the fraction γ/η , we get

$$M(m) = 2\pi[1 + 3(m - \phi_2/2\pi)], \quad (\text{A9a})$$

$$N(n) = 2\pi[2 + 3(n - \phi_3/2\pi)],$$

and for the fraction ζ/κ , we instead have

$$M(m) = 2\pi[2 + 3(m - \phi_2/2\pi)], \quad (\text{A9b})$$

$$N(n) = 2\pi[1 + 3(n - \phi_3/2\pi)].$$

Examination of these expressions reveals that a 2π change in relative phases ϕ_2 or ϕ_3 may be absorbed as an integer change in the associated parameter-space coordinate m or n respectively. By allowing m and n to correspond to discrete real values instead of integer values, they may then also absorb fractional parts of the relative phase. Consequently, the vortex lattice may be continuously translated by a single lattice cell for each 2π change in the source phase. The position of any vortex in a cell coinciding with the BEC trap center is thus understood as resulting from a translation of the entire lattice. Isolating θ in Eq. (A8) yields

$$\theta = \arctan \left[\frac{1}{\sin \theta_3} \left(\frac{r_3 - \beta N(n)/r_3}{r_2 - \beta M(m)/r_2} \right) - \cos \theta_3 \right]. \quad (\text{A10})$$

Finally, the expression for the radial coordinate r of the (m, n) th vortex core is obtained from Eq. (A6a) or Eq. (A7a) by applying the identity $\cos^2 \theta = 1/(1 + \tan^2 \theta)$ and making use of Eq. (A10):

$$r = \frac{1}{2} \sqrt{\frac{1}{\sin^2 \theta} \left[r_3 - \frac{\beta N(n)}{r_3} - \left(r_2 - \frac{\beta M(m)}{r_2} \right) \cos \theta_3 \right]^2 + 1}. \quad (\text{A11})$$

Together with Eq. (A10), we have the vortex coordinates (r, θ, t) , with the sign of the vortex charge—i.e. whether they describe the positions of vortices or antivortices—depending on the choice of Eqs. (A9a) or (A9b) and the value of θ_3 . If $\theta_3 \in (0, \pi)$, vortices are indicated by Eq. (A9a) and antivortices by Eq. (A9b). If $\theta_3 \in (\pi, 2\pi)$, the association is reversed, with vortices indicated by Eq. (A9b) and antivortices by Eq. (A9a).

Note that, in contrast with the case described in [12], in which the allowed range of integers (m, n) was restricted, here there are no restrictions and an infinite, uniform vortex–antivortex lattice is generated. However, the amplitude term Eq. (A3) applies a Gaussian envelope to the probability density $|\Psi|^2 = \left| \sum_{j=1}^3 A_j(\mathbf{r}) \right|^2$, effectively limiting the lattice. For sources arranged at the three corners of an equilateral triangle, the lattice has a symmetric honeycomb symmetry, with regular hexagonal cells. Changing the angle θ_3 , or the side lengths r_2 or r_3 , distorts the cells and the lattice.